

Organized Chaos: Scatter in the relation between stellar mass and halo mass in small galaxies

Shea Garrison-Kimmel^{1*}, James S. Bullock², Michael Boylan-Kolchin³,
Emma Bardwell⁴

¹*TAPIR, California Institute of Technology, Pasadena, CA 91125, USA*

²*Center for Cosmology, Department of Physics and Astronomy, University of California, Irvine, CA 92697, USA*

³*Department of Astronomy, The University of Texas at Austin, 2515 Speedway, Stop C1400, Austin, TX 78712*

⁴*Case Western Reserve University, Cleveland, Ohio 44106, USA*

2 November 2016

ABSTRACT

We use Local Group galaxy counts together with the ELVIS N-body simulations to explore the relationship between the scatter and slope in the stellar mass vs. halo mass relation at low masses, $M_\star \simeq 10^5 - 10^8 M_\odot$. Assuming models with log-normal scatter about a median relation of the form $M_\star \propto M_{\text{halo}}^\alpha$, the preferred log-slope steepens from $\alpha \simeq 1.8$ in the limit of zero scatter to $\alpha \simeq 2.6$ in the case of 2 dex of scatter in M_\star at fixed halo mass. We provide fitting functions for the best-fit relations as a function of scatter, including cases where the relation becomes increasingly stochastic with decreasing mass. We show that if the scatter at fixed halo mass is large enough ($\gtrsim 1$ dex) *and* if the median relation is steep enough ($\alpha \gtrsim 2$), then the “too-big-to-fail” problem seen in the Local Group can be self-consistently eliminated in about $\sim 5 - 10\%$ of realizations. This scenario requires that the most massive subhalos host unobservable ultra-faint dwarfs fairly often; we discuss potentially observable signatures of these systems. Finally, we compare our derived constraints to recent high-resolution simulations of dwarf galaxy formation in the literature. Though simulation-to-simulation scatter in M_\star at fixed M_{halo} is large among separate authors (~ 2 dex), individual codes produce relations with much less scatter and usually give relations that would over-produce local galaxy counts.

Key words: dark matter – cosmology: theory – galaxies: halos – Local Group

1 INTRODUCTION

The standard paradigm of galaxy formation posits that dark matter halos are the sites of galaxy formation (White & Rees 1978; Blumenthal et al. 1984). The underlying relationship between galaxies and dark matter halos has emerged as an important benchmark for detailed theories. In particular, reproducing the observed abundance of galaxies as a function of stellar mass or luminosity imposes a particularly powerful constraint on models (Klypin et al. 1999; Benson et al. 2000; Bullock et al. 2002; Berlind & Weinberg 2002; Kravtsov et al. 2004).

Perhaps the simplest example of this approach is to assume that more massive dark matter halos host brighter galaxies, such that the cumulative number density of dark matter halos matches the cumulative number density of

galaxies in a nearly one-to-one fashion. On large scales and for bright galaxies, this abundance matching (AM) assumption, when applied using cosmological, DM-only simulations, yields clustering statistics that agree remarkably well with observations for $\sim L_\star$ galaxies with $M_\star \simeq 10^{10-11}$ (Conroy et al. 2006; Reddick et al. 2013). Moreover, observational estimates for halo masses, e.g. from X-ray temperatures or virial-scale satellite kinematics, agree well with AM relations up to the scale of giant cluster galaxies $M_\star \simeq 10^{12} M_\odot$ (e.g. Kravtsov et al. 2014). AM even appears to work well down to $M_\star \sim 10^9 M_\odot$: when applied to the Millennium-II simulation (Boylan-Kolchin et al. 2009), it correctly reproduces not only the fraction of Milky Way (MW)-size hosts with LMC-size satellites, but also the radial and velocity distributions of those satellites (Tollerud et al. 2011). Perhaps most surprisingly, galaxies over this range ($M_\star \simeq 10^{9-12} M_\odot$) appear to populate halos with a fairly small amount of scatter at fixed halo mass. Behroozi et al. (2013c), for example, report a log-normal scatter (one standard deviation) of 0.2 dex in

* sheagk@caltech.edu

M_* at fixed M_{halo} . Reddick et al. (2013) also prefer 0.2 dex of scatter based on their clustering analysis. Kravtsov et al. (2014) quote 0.1 dex for brightest cluster galaxies.

The focus of the present work is to explore the relationship between halos and galaxies below the stellar mass range that is easily accessible in large, volume-limited surveys: $M_* < 10^8 M_\odot$. Simply extrapolating the slope of the relationship reported at higher masses would suggest that dwarf galaxies obey a relation $M_* \propto M_{\text{halo}}^\alpha$, with $\alpha \simeq 1.6 - 1.9$ (Behroozi et al. 2013c; Moster et al. 2013). In fact, Garrison-Kimmel et al. (2014a) found that this assumption with $\alpha = 1.9$ and minimal scatter does reproduce the abundance of Local Group (LG) galaxies down to $M_* \simeq 10^6 M_\odot$ reasonably well. In contrast, Brook et al. (2014) performed a similar analysis and found a preferred log-slope of $\alpha = 3.1$ over the tight mass range $M_* \simeq 10^{6-8} M_\odot$. This is much steeper than the relationship one expects from extrapolating the trend seen at higher masses. However, the log-slope obtained by Brook et al. (2014) is degenerate with the normalization at high masses ($M_* \sim 10^{9.5} M_\odot$), which, due to their method of matching simulated halo mass functions to the observed stellar mass function, is sensitive to the masses of the largest halos that form in their Local Group environments. In fact, Brook et al. (2014) predict very similar halo masses to the Garrison-Kimmel et al. (2014a) relation for $M_* \sim 10^6 - 10^7 M_\odot$.

While AM (with minimal scatter) can reasonably reproduce the counts of local galaxies, there are reasons to consider the possibility that it breaks down entirely at very low masses, or at least that the scatter increases dramatically. One motivation comes from galaxy formation physics, which suggests that star formation and gas retention in small halos may be very sensitive to small changes in the halo’s virial temperature and mass-accretion history reaching back to the epoch of reionization (Bullock et al. 2000; Somerville 2002; Oñorbe et al. 2015; Sawala et al. 2016). Another clue comes from direct mass measurements in small galaxies themselves. The smallest satellite galaxies of the MW demonstrate no observable trend between central dynamical mass and luminosity (Strigari et al. 2008), which may suggest that there is no trend between total halo mass and stellar mass (or at least that the relationship is very steep). A related result was presented by Boylan-Kolchin et al. (2011, 2012), who compared the central masses of dark matter subhalos in the ultra-high resolution Aquarius simulations of MW-size hosts (Springel et al. 2008a) to the masses of the bright MW dwarf spheroidals (dSphs). They found that the largest subhalos are denser than any of the known MW dwarfs. One interpretation could be that the most massive predicted subhalos have simply failed to form enough stars for them to be observable, but given the comparatively high mass of the offending halos (well above the mass where photoionization is expected to act) we expect the missing halos to be “too big to fail” (TBTF).

A wide variety of solutions for TBTF have been proposed. For example, di Cintio et al. (2011), Wang et al. (2012), Boylan-Kolchin et al. (2012), and Vera-Ciro et al. (2013) pointed out that reducing the assumed mass of the MW host halo to $M_{\text{halo}} \sim 8 \times 10^{11} M_\odot$ will reduce the number of problematic subhalos. It is also possible that the substructure population of the MW is abnormal for its mass (Purcell & Zentner 2012; Rodríguez-Puebla et al. 2013;

Garrison-Kimmel et al. 2014b), though the fact that the same problem appears to exist around M31 (Tollerud et al. 2014) makes such a solution less appealing. The detailed analysis of Jiang & van den Bosch (2015) strongly suggests that such a case would be exceedingly rare.

Others (e.g. Zolotov et al. 2012; Brooks et al. 2013; Araki et al. 2014; Del Popolo et al. 2014) have argued that interactions with the baryons in the host galaxy, which are not included in dark-matter only simulations, act to reduce the central densities of the massive failures such that their integrated masses within ~ 1 kpc are similar to those of the MW dSphs. Similarly, Read et al. (2006) used idealized N-body simulations to demonstrate that tidal shocking may lower the central velocity dispersions of dwarf halos if the halos are accreted with cored profiles. These solutions, however, are only applicable within the virial radius (R_v) of the MW, and break down when faced with the ubiquity of TBTF not only in the nearby field (Garrison-Kimmel et al. 2014b), but also well beyond the LG (Papastergis et al. 2015; Papastergis & Shankar 2016).

Other authors have proposed explanations for TBTF that do not rely on environmental influences, and which could therefore act even in the field. Gas blowouts, driven by supernovae events within the dwarfs, may add energy to dark matter particle orbits and reduce the central densities enough to match observations (Navarro et al. 1996; Mashchenko et al. 2008; Pontzen & Governato 2012; Governato et al. 2012; Brooks & Zolotov 2014; Amorisco et al. 2014; Gritschneider & Lin 2013). Though many authors (Gnedin & Zhao 2002; Peñarrubia et al. 2012; Garrison-Kimmel et al. 2013; di Cintio et al. 2014) have argued that the galaxies of interest ($M_* \lesssim 10^6 M_\odot$) do not produce enough supernovae to drive the required blowouts, other authors (e.g. Read & Gilmore 2005; Maxwell et al. 2015) have made the point that energetic arguments depend crucially on just how the dark matter particle orbits are perturbed. Oñorbe et al. (2015) presented a single simulation of a $M_* \sim 2 \times 10^6 M_\odot$ galaxy that formed within a TBTF halo with a central core density consistent with those observed for similarly sized dwarfs. Read et al. (2016a,b) used idealized simulations to argue that these cores form in halos as small as $M_{\text{halo}} = 10^8 M_\odot$, though their simulations form ~ 10 times more stars than AM extrapolations predict. It is not clear whether core formation of this kind should be common enough to resolve the problem generally.

More recently, Papastergis & Shankar (2016) have used HI data to show that the mass deficit exists at radii well beyond the stellar extent of the galaxy. This is particularly hard to reconcile in models where stellar-feedback driven core formation solves TBTF in energetically feasible ways (di Cintio et al. 2014; Oñorbe et al. 2015; Maxwell et al. 2015; Chan et al. 2015). This is because the dark matter cores produced by supernovae explosions in these cosmological simulations are typically similar in size to the stellar half-light radius of the galaxy.¹

¹ Garrison-Kimmel et al. (2013) used simple numerical experiments to explore models that removed dark matter mass well beyond the galaxy half-light radius, but showed that these cases require even more energy, likely exceeding the energy budget available from supernovae.

Concerns about the ability of baryonic physics to resolve TBTF have motivated solutions that are cosmological in nature. These include modifications to the small-scale power spectrum (Polisensky & Ricotti 2014; Garrison-Kimmel et al. 2014c) and altering the assumption that dark matter is both cold (Anderhalden et al. 2013; Lovell et al. 2014; Horiuchi et al. 2016; Bozek et al. 2016) and collisionless (Vogelsberger et al. 2012; Rocha et al. 2013; Zavala et al. 2013; Elbert et al. 2015).

Most of the explanations detailed above alter the density profiles of massive (sub)halos such that they may host the observed dwarfs. In principle, however, these massive dwarf halos may remain cuspy and dense but form far fewer stars than simple, low-scatter extrapolations of AM relations suggest. In such a situation, a TBTF halo would not be “too big to fail” after all, but actually remain undetectable to current observations. In practice, therefore, TBTF may be indicative of increased scatter in the M_\star - M_{halo} relation at small masses. If so, this would indicate that galaxy formation proceeds in a fundamentally distinct way in dark matter halos smaller than $M_{\text{halo}} \sim 10^{11} M_\odot$, perhaps because the baryons in those potential wells are far more susceptible to both internal and external perturbations than previously expected. Understanding the scatter in the M_\star - M_{halo} relation is thus crucial to our overall understanding of how stars and galaxies form in dark matter halos.

In what follows, we use the ELVIS (Exploring the Local Volume in Simulations) suite (Garrison-Kimmel et al. 2014a) along with the stellar mass function (SMF) of galaxies in the Local Group (LG) to constrain the M_\star - M_{halo} relation down to the lowest stellar masses possible due to completeness $M_\star \simeq 10^5 M_\odot$. We normalize our relation at high masses to the results of Behroozi et al. (2013c, hereafter B13) and explore models with a variable faint-end log-slope α and a log-normal scatter σ and explore the covariance between them.

This paper is organized as follows: §2 discusses the observational and theoretical data employed here, followed by the methods for assigning stellar masses to (sub)halos and quantifying the goodness of fit to the M_\star functions. §3 presents the best-fit log-slope, and explores one impact of varying the scatter by investigating the severity of TBTF, quantified by the number of “bright” massive failures in each realization. We close by discussing other observable consequences of an increase in the low mass scatter in §4 and briefly summarize in §5.

2 METHODS

2.1 Observational Data

In order to maximize the observational sample size, we adopt three independent completeness cuts for dwarfs that are either 1) satellites of the Milky Way; 2) satellites of M31; or 3) non-satellite that exist within in the Local Group. We include all eleven classical satellites of the MW, defined as those identified prior to SDSS within 300 kpc of the Galactic center. The faintest of these, Draco, defines our incompleteness limit of $M_\star = 4.5 \times 10^5 M_\odot$. Completeness around M31 is perhaps better understood due to the uniformity of the PAndAS survey – Figure 24 of Tollerud

et al. (2012) illustrates that PAndAS is complete to galaxies with half-light luminosities $L_{1/2} > 10^5 L_\odot$, for typical half-light radii.² Assuming a mass-to-light ratio of two, consistent with the findings of Martin et al. (2008) and with extrapolations of the Bell & de Jong (2001) relations to the dwarf scale, and including the total stellar mass of the galaxy, we therefore adopt an incompleteness limit of $M_\star = 10^5 M_\odot$, but only include galaxies (and subhalos) within the PAndAS footprint, the central 150 kpc of the galaxy. In the “Local Field” (LF), defined here as the region more than 300 kpc from both the MW and M31, but within 1.2 Mpc of either (a cut chosen to match the possible cuts in the simulations; see §2.2), we adopt an incompleteness limit of $M_\star = M_{\star, \text{Cetus}} = 4.5 \times 10^6 M_\odot$. We acknowledge, however, that incompleteness in the LF is poorly understood, and we therefore analyze the LF separately from the satellite populations.

We exclude the two most massive satellites of both the MW (the LMC and the SMC) and M31 (M33 and NGC 205) from our analysis because such luminous satellites are known to be rare around MW-size systems (Boylan-Kolchin et al. 2010; Busha et al. 2011; Tollerud et al. 2011), and many of the ELVIS hosts lack the massive subhalos that appear to host these systems (Tollerud et al. 2011); including these systems, however, has only a slight effect on the results. Halos assigned stellar masses below the completeness limit are not considered in calculating the goodness-of-fit between the observational SMFs and those derived from the simulations (see §2.4). Many models therefore overproduce counts below the cited completeness limits. If there are undiscovered galaxies *above* the completeness limits, then we will underestimate the best-fit log-slope.

The names, stellar masses, and adopted distances from the centers of the MW and M31 are listed in Table 1; we explicitly note that our distance cuts exclude M33 (Triangulum), which lies outside the PAndAS footprint. The anti-cumulative stellar mass functions are also plotted in Figure 1 for the MW (magenta), M31 (cyan), and in the LF (orange), with the individual galaxies labeled. Stellar masses are drawn from Woo et al. (2008) where possible, and are otherwise calculated from the data in McConnachie (2012), assuming $M_\star/L = 2$. Similarly, the MW-centric distances are taken from McConnachie (2012), and the M31-centric distances are calculated from the positions given in that work, assuming an MW-M31 separation of 787 kpc (McConnachie et al. 2005).

2.2 Simulations

Subhalo and field halo mass functions are drawn from the Exploring the Local Volume In Simulations (ELVIS) suite, detailed in full in Garrison-Kimmel et al. (2014a). Briefly, ELVIS includes twelve LG-like MW/M31 pairs of hosts, selected to be ~ 800 kpc apart, moving towards one another, and isolated from any larger systems. ELVIS additionally includes twenty-four isolated hosts, mass-matched to the

² If, however, more spatially extended galaxies ($R_{1/2} > 1$ kpc) are common, then we are under-estimating the completeness, and would therefore over-estimate the steepness of the $M_\star - M_{\text{halo}}$ relation.

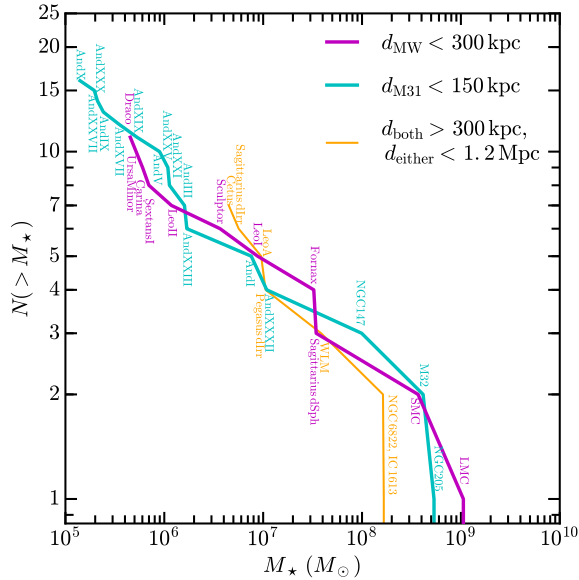


Figure 1. The stellar mass functions of the classical MW satellites (magenta), the M31 satellites within the PAndAS survey volume ($d_{M31} < 150$ kpc, cyan), and galaxies in the Local Field (orange), which includes all galaxies more than 300 kpc from both the MW and M31, but within 1.2 Mpc of either giant. Stellar masses are from [Woo et al. \(2008\)](#), where available, and are otherwise calculated from the luminosities tabulated in [McConnachie \(2012\)](#), assuming a mass-to-light ratio of two. Each histogram is truncated at the adopted completeness limit: $M_* = M_{*,\text{Draco}} = 4.5 \times 10^5 M_\odot$ for the MW satellites, $M_* = 10^5 M_\odot$ for satellites around M31 ([Tollerud et al. 2012](#)), and $M_* = 4.5 \times 10^6 M_\odot$ in the Local Field.

systems in the pairs. All systems are free of contaminating low-resolution (high mass) particles within their virial radii. Moreover, the fields around the paired halos are uncontaminated within $\gtrsim 1$ Mpc of each halo center: only four pairs contain low resolution particles within 1.2 Mpc of a host center, and the low-resolution mass fraction within that volume is $\ll 0.1\%$ in each of those systems. We therefore define the “Local Field” (LF) as the volume within 1.2 Mpc of either host center, but more than 300 kpc from both hosts (as in [Garrison-Kimmel et al. 2014a](#)).

The ELVIS suite was initialized using MUSIC ([Hahn & Abel 2011](#)) and simulated using a combination of GADGET-2 and GADGET-3 ([Springel 2005](#)) assuming WMAP-7 cosmological parameters ([Larson et al. 2011](#)): $\Omega_m = 0.266$, $\Omega_\Lambda = 0.734$, $n_s = 0.963$, $\sigma_8 = 0.801$, and $h = 0.71$. All forty-eight halos were simulated with high-resolution regions embedded within boxes 70.4 Mpc on a side. The particle mass m_p within that high-resolution volume is $1.9 \times 10^5 M_\odot$; the Plummer-equivalent force softening ϵ is held fixed in comov-

Name	M_* (M_\odot)	d_{MW} (kpc)	d_{M31} (kpc)
MW satellites ($d_{\text{MW}} < 300$ kpc)			
LMC	1.06×10^9	50	811
SMC	3.69×10^8	61	812
Sagittarius dSph	3.44×10^7	19	792
Fornax	3.25×10^7	149	773
Leo I	8.79×10^6	257	922
Sculptor	3.67×10^6	86	766
Leo II	1.18×10^6	236	902
Sextans I	6.98×10^5	89	839
Carina	6.03×10^5	107	842
Ursa Minor	4.53×10^5	78	758
Draco	4.53×10^5	76	755
M31 satellites ($d_{\text{M31}} < 150$ kpc)			
NGC 205	5.35×10^8	828	42
M32	4.15×10^8	809	23
NGC 147	9.91×10^7	680	143
Andromeda XXXII	1.09×10^7	780	141
Andromeda I	7.59×10^6	749	58
Andromeda XXIII	1.69×10^6	774	126
Andromeda III	1.6×10^6	752	75
Andromeda XXI	1.13×10^6	831	134
Andromeda XXV	1.09×10^6	817	89
Andromeda V	8.96×10^5	777	110
Andromeda XIX	5.3×10^5	824	114
Andromeda XVII	3.47×10^5	732	70
Andromeda IX	2.42×10^5	770	41
Andromeda XXX	2.11×10^5	686	148
Andromeda XXVII	1.96×10^5	832	74
Andromeda X	1.41×10^5	674	139
Local Field Galaxies			
NGC 6822	1.66×10^8	452	898
IC 1613	1.63×10^8	758	520
WLM	3.86×10^7	933	836
Pegasus dIrr	1.06×10^7	921	474
Leo A	9.55×10^6	803	1200
Sagittarius dIrr	5.65×10^6	1059	1357
Cetus	4.49×10^6	756	680

Table 1. The names of galaxies included in this work, along with their adopted stellar masses and distances from the MW and M31. The sample includes the classical satellites of the MW, dwarfs with $M_* \geq 10^5 M_\odot$ within 150 kpc of M31, and galaxies brighter than Cetus in the LF. Stellar masses are taken from [Woo et al. \(2008\)](#) where available, and are otherwise drawn from the data compiled in [McConnachie \(2012\)](#), assuming a mass-to-light ratio of two. MW-centric distances are also drawn from [McConnachie \(2012\)](#) and M31-centric distances are calculated assuming a MW-M31 separation of 787 kpc ([McConnachie et al. 2005](#)).

ing units for $z > 9$, after which ϵ becomes 141 pc in physical units.³

³ Three of the isolated halos were also simulated with eight times more particles in the high-resolution regions ($m_p = 2.35 \times 10^4 M_\odot$, $\epsilon = 70.4$ pc). [Garrison-Kimmel et al. \(2014a\)](#) used these simulations to show that the ELVIS suite is complete to $M_{\text{peak}} = 6 \times 10^7 M_\odot$, which is well below the adopted observational completeness cut for the vast majority of the models that we explore here: for $\alpha = 2$, e.g., $M_*(M_{\text{peak}} = 6 \times 10^7 M_\odot) \sim 10^2 M_\odot$. However, numerical incompleteness in the halo catalog may influence our results for large scatters and/or very shallow slopes. We therefore calculate the best-fit log-slopes, derived from comparing realizations drawn from those three isolated halos to the stellar

Following B13, we parameterize the M_\star - M_{halo} relation in terms of M_{peak} , the largest instantaneous virial mass associated with the main branch of each (sub)halo’s merger tree. Particularly for subhalos, which have been significantly stripped via interactions with the MW/M31 host, “peak” quantities appear to correlate more strongly with M_\star than the subhalo properties today (Reddick et al. 2013). Peak quantities for the ELVIS halos are drawn from merger trees created with `rockstar` (Behroozi et al. 2013a) and `consistent-trees` (Behroozi et al. 2013b; for more details, see Garrison-Kimmel et al. 2014a).

In order to create an analogous comparison set to the observational data, we create satellite populations within both 150 kpc and 300 kpc of each ELVIS halo center for every combination of α and σ . The former (latter) population is then compared to the M31 (MW) dataset. To find a final goodness-of-fit, each ELVIS pair is compared to the paired observational dataset, where the better fit matching between the two halos and the MW/M31 is used in each realization. Because the isolated ELVIS hosts have mass functions that are indistinguishable from those of the paired hosts (Garrison-Kimmel et al. 2014a), we create “pairs” from the isolated hosts to maximize our simulation sample; the isolated halos, however, are excluded from the LF analysis. Furthermore, the fields around three of the ELVIS pairs (Siegfried & Roy, Serena & Venus, and Kek & Kauket) are systematically offset to much higher masses at fixed number, compared to the remaining nine pairs. These systems thus prefer extremely steep log-slopes ($\alpha \gtrsim 4$) at all scatters to avoid overproducing the LF SMF. We therefore eliminate them from our LF analysis because they do not appear to be representative of the field around the MW.

2.3 Assigning stellar masses to halos

We explore monotonic relationships between M_\star and M_{peak} with log-normal symmetric scatter σ in M_\star at fixed M_{peak} . The models match the results of B13 above the dwarf scale: for $M_{\text{peak}} > M_1 \sim 10^{11.5} M_\odot$ (roughly the mass at which the low-mass slope begins to dominate), we directly adopt the median relation in B13. We emphasize that the stellar mass predicted at M_1 , $M_\star \sim 5 \times 10^9 M_\odot$, roughly matches the stellar mass of the LMC, $\sim 10^9 M_\odot$. As noted above, the population statistics of LMC-size galaxies are reproduced well with minimal scatter in AM relations, but both simulations and observations suggest that different physical processes may become important on smaller scales. We therefore allow both the log-slope and the scatter to vary freely for $M_{\text{peak}} < M_1$.

Specifically, B13 parameterizes $M_\star(M_{\text{halo}})$ as

$$\log_{10} M_\star = \log_{10}(\epsilon M_1) + f(\log_{10}(\frac{M_{\text{halo}}}{M_1})) - f(0) \quad (1)$$

where

$$f(x) = -\log_{10}(10^{-\alpha x} + 1) + \delta \frac{(\log_{10}(1 + \exp(x)))^\gamma}{1 + \exp(10^{-x})}. \quad (2)$$

mass function of the MW, both at the fiducial resolution and at higher resolution. Averaged over 500 realizations, the best-fit α differs by $\sim 6\%$ at most, indicating that our results are independent of numerical resolution.

A full interpretation of the parameters, which vary with redshift, is given in Table 1 of B13; briefly, M_1 and ϵ indicate the characteristic halo mass and stellar mass to halo mass ratio, respectively, while γ and δ govern the behavior at the high mass end ($M_{\text{halo}} > M_1$). For our purposes, however, the low mass end is most important, where Equation 1 behaves as a power-law with log-slope α : $M_\star \propto M_{\text{halo}}^\alpha$. In the analysis that follows, we hold the parameters quoted in Section 5 of B13 fixed for $M_{\text{halo}} > M_1$, but replace α with values ranging freely from 0 to 4 for $M_{\text{halo}} < M_1$. For comparison, B13 derive a faint-end log-slope $\alpha = 1.412$ at $z = 0$, though Garrison-Kimmel et al. (2014a) showed that $\alpha = 1.92$ better reproduces galaxy counts in the LG with the same normalization, assuming zero scatter. Below, however, we demonstrate explicitly that the best-fit α varies monotonically with the assumed scatter.

We primarily explore two models for including scatter in the $M_\star - M_{\text{halo}}$ relation. The first, which we refer to as “constant scatter,” assumes a symmetric, log-normal scatter σ in M_\star at fixed M_{peak} that is independent of M_{peak} . This model is based on the results of B13, who quote a constant σ of 0.2 dex for $M_\star > 10^{8.5} M_\odot$. Rather than introducing a discontinuity in the scatter at $M_\star = 10^{8.5} M_\odot$, we elect to apply scatter uniformly at all M_{peak} . Due to a lack of galaxies in our observational sample with $M_\star \gtrsim 10^9 M_\odot$ and a lack of (sub)halos with $M_{\text{peak}} \gtrsim 10^{11} M_\odot$ (Figures 3 and 5 of Garrison-Kimmel et al. 2014a), however, our method primarily constrains the scatter below the masses probed by B13.

Our second model, which we refer to as the “growing scatter” model, is motivated by recent simulation results that suggest the level of stochasticity in galaxy formation may increase at decreasing halo masses (e.g. Sawala et al. 2016). Specifically, we model the log-normal scatter σ as a function of the peak mass, such that $\sigma = 0.2$ for $M_{\text{peak}} > M_1$ but grows linearly with decreasing $\log_{10} M_{\text{peak}}$ for $M_{\text{peak}} \leq M_1$:

$$\sigma_v = 0.2 + v \times (\log_{10} M_{\text{peak}} - \log_{10} M_1). \quad (3)$$

The parameter v quantifies the rate at which the scatter grows: a more negative v (larger magnitude) results in larger scatter at fixed M_{peak} , whereas $v = 0$ corresponds to a constant scatter of 0.2 dex.

For both models, we create 500 realizations for each satellite or field system, resulting in 12,000 “paired” realizations of the satellite systems of the MW and M31 and 4500 realizations of the LF for every combination of α and σ .

Though we do not present the results here, we also explore a model with a sharp cut-off in star formation below $M_{\text{peak}} = 10^9 M_\odot$, as motivated by reionization arguments (Bullock et al. 2000; Somerville 2002) and recent hydrodynamic simulations (e.g. Sawala et al. 2016, but see Wheeler et al. 2015). The results from such a model are nearly identical, however, as the galaxies included in our sample are nearly always assigned to halos with $M_{\text{peak}} > 10^9 M_\odot$. Moreover, the dark systems predicted in Sawala et al. (2016) arise naturally from power-law models with scatter, provided the scatter is large enough that (sub)halos can be assigned no stellar mass. We additionally explore models with one-sided scatter, including both exponential and Rayleigh distributions; models with fixed $\sigma = 0.2$ dex above $M_1 \sim 10^{11.5} M_\odot$; models that break from the B13 relation at

$M_{\text{halo}} = 10^{10.5} M_{\odot}$; and models with M_{\star} fixed to be less than $M_{\text{peak}} \times f_{\text{b}}$, the cosmic baryon fraction. All of these yield very similar results to the two simple models described above. In principle, the $M_{\star} - M_{\text{halo}}$ relation may not be well-described by scatter about a power-law. Without clear evidence of another functional form, however, we elect to explore extrapolations of an AM relation that reproduces the data at larger M_{\star} .

2.4 Quantifying the goodness of fit

We now turn to the problem of quantifying the match between a theoretical realization for the stellar mass function and the true observational SMF. Rather than performing a likelihood-based analysis on the differential mass functions, which is sensitive to the choice of bins due to the small numbers of objects, we elect to compare the mass functions in an anti-cumulative sense. Specifically, for each realization, we rank-order the galaxies by stellar mass and calculate

$$\kappa = \frac{1}{N} \sum_{i=1}^N \left| \log_{10} \left(M_{\star, i}^{\text{theory}} \right) - \log_{10} \left(M_{\star, i}^{\text{data}} \right) \right|. \quad (4)$$

That is, κ for a single realization is the average difference (in log-space) between the i -th brightest galaxy in the observational sample and the i -th brightest galaxy in that realization.⁴ The best-fit log-slope for a given σ is therefore that which minimizes κ .

In order to evaluate κ as a metric, we compare the fiducial stellar masses listed in Table 1 to Monte Carlo realizations of the data themselves created by sampling log-normal distributions on their reported observational errors in the stellar masses (where the errors are again drawn from the data cataloged in [McConnachie 2012](#)). The values of κ calculated this way vary between ~ 0.05 dex and ~ 0.2 dex, peaking at ~ 0.11 dex, for both the MW and M31 satellite systems. The LF sample, by virtue of the high completeness cut (and smaller errors on M_{\star}), peaks at ~ 0.06 dex. We conclude that theoretical realizations with $\kappa \sim 0.2$ dex are very similar to the observed stellar mass function, roughly consistent with randomly sampling the data themselves within observational errors.

Because κ takes into account only the N “brightest” halos in a given realization, where N is the number of galaxies in the corresponding observational sample, it does not constrain the shape of the stellar mass function below the faintest galaxy in the observational sample. This fact is inconsequential for the MW and LF samples, as the incompleteness limit is defined by M_{\star} of the faintest galaxy, but it is important for M31, where the incompleteness is better understood. To therefore constrain the shape of the stellar mass function between the incompleteness limit, $10^5 M_{\odot}$, and the faintest galaxy in the sample, $\sim 1.5 \times 10^5 M_{\odot}$, we insert a galaxy with $M_{\star} = 10^5 M_{\odot}$ into the catalog; that is,

⁴ We also explore alternative definitions of κ , including a version without the absolute value (such that differences may cancel out) and a root-mean-square method, which highlights the largest discrepancies. Overall, we find that the best-fit slopes are nearly identical between the definitions when averaging over the realizations of a simulated system, regardless of the specific definition of κ .

we assume there is an undetected galaxy lurking just below the completeness limit. Without this insertion, κ generally prefers slightly steeper slopes, but the models predict additional galaxies with $M_{\star} \sim 10^5 M_{\odot}$ within the PAndAS footprint.⁵

3 RESULTS

One of the qualitative aims of this paper is to accurately explore the covariance between scatter and slope. The basic need for this is illustrated in Figure 2. The left panel shows two example relations between stellar mass and halo mass: one, in cyan, with a steep slope ($M_{\star} \propto M_{\text{halo}}^{\alpha}$ with $\alpha = 2.6$) and large scatter ($\sigma = 2$ dex), and the other, in magenta, with a flatter slope ($\alpha = 1.8$) and no scatter. The right panel presents the resultant stellar mass functions from averaging over realizations of the ELVIS halos (along with those observed for the MW and M31 combined (see §2.1 and Table 1 for details)). Both of these models produce similar stellar mass functions (which are roughly consistent with those observed in the Local Group) even though their slopes are significantly different. This is driven by the difference in scatter. The dashed cyan line the right panel assumes the same steep relation as the solid line, but this time with zero scatter; this results in a satellite mass function that is much below the data. This difference is due to the rapidly rising halo mass function. In cases with a large amount of scatter, small systems scattering to large stellar masses will dominate over large systems scattering to low stellar masses. Intuitively, therefore, large scatter requires a steeper slope to avoid overproducing the observed stellar mass function.

In what follows we present a more rigorous analysis to jointly constraint the scatter and slope.

3.1 Relation between log-slope and scatter

We begin by examining the best-fit log-slope α at each assumed scatter σ , both within the virialized volumes of the host halos and in the fields surrounding them. Figure 3 shows the fit parameter κ as a function of slope α and scatter for the satellites of the MW and M31 on the left and galaxies in the Local Field (LF) on the right. The results have been averaged over all simulations, including 500 realizations of each simulation for each (α, σ) model represented on the grid. In the left panel, we choose the smaller of $(\kappa_{\text{MW, host 1}} + \kappa_{\text{M31, host 2}})/2$ and $(\kappa_{\text{MW, host 2}} + \kappa_{\text{M31, host 1}})/2$ for each realization, intrinsically allowing the MW/M31 to be matched with either the larger or smaller ELVIS host.⁶

The solid white line in Figure 3 indicates the average best-fit α for the satellite systems; i.e., it plots the minimum

⁵ The number of “fake” galaxies inserted, however, is relatively unimportant: adding ten galaxies with $M_{\star} = 10^5 M_{\odot}$ into the catalogs changes the results by a negligible amount.

⁶ Only one “pair” strongly prefers to match the MW with the larger host at all σ , whereas several prefer to match the MW with the lower mass host. However, for $\sigma \gtrsim 0.25$, many systems have roughly an equal probability to match the MW with each host. Together, these conspire to keep the mean fraction of realizations where the MW is matched with the larger host nearly constant at $\sim 30\%$.

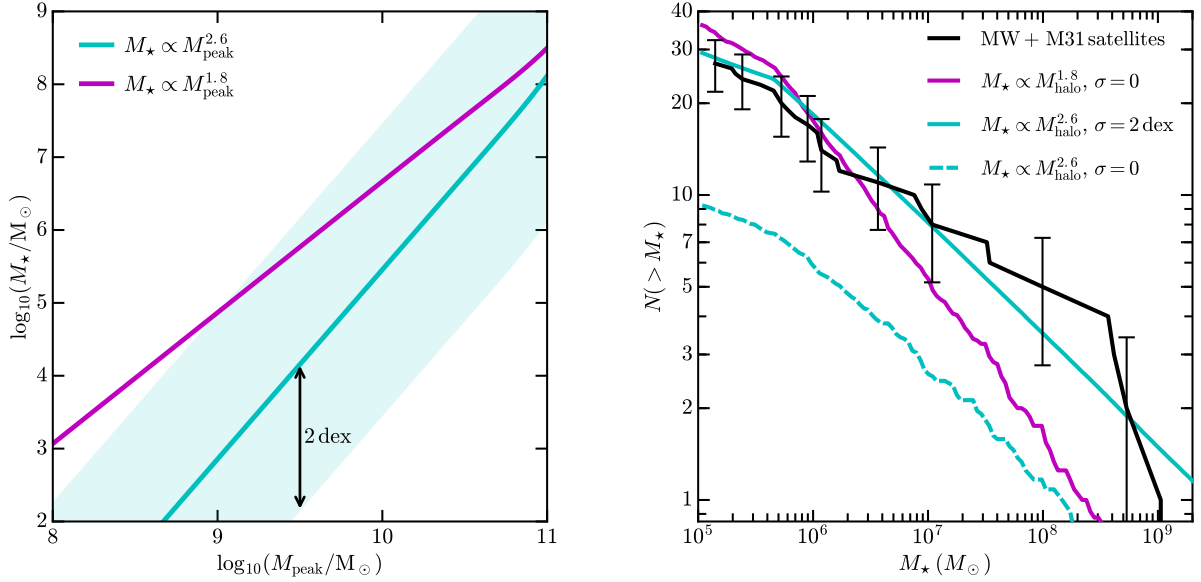


Figure 2. *Left:* Two sample relations between (sub)halo mass, quantified here by M_{peak} , the largest mass a (sub)halo ever attains, and galaxy stellar mass M_\star at $z = 0$. Both relations are anchored to the Behroozi et al. (2013c) relation above $M_{\text{peak}} \sim 10^{11.5}$. The magenta line plots a relation that at the faint end asymptotes to $M_\star \propto M_{\text{halo}}^\alpha$ with $\alpha = 1.8$ (similar that advocated in Garrison-Kimmel et al. 2014a) and with no scatter. The cyan line shows an alternative, steeper relation, with $\alpha = 2.6$, but with correspondingly larger scatter $\sigma = 2$ dex. *Right:* In black, the anti-cumulative stellar mass function (SMF) of the MW and M31 satellites used in this work (see §2.1), with Poissonian error bars. The magenta line plots the mean of the SMFs obtained from applying the magenta line in the right plot to the ELVIS subhalo populations. Similarly, the solid cyan line plots the mean SMF obtained by assuming the cyan relation in the right plot, including a log-normal scatter of 2 dex. The dotted cyan line, however, represents the mean SMF from the same relation, but without applying any scatter. The break at $M_\star \sim 10^{5.5} M_\odot$ is due to the completeness cut placed on the MW satellites. There is clearly a degeneracy between the slope of the M_\star - M_{halo} relation and the assumed scatter, such that one must vary both to maintain a good fit to the local SMFs.

κ in the left panel. The two regions yield qualitatively similar results, though the LF prefers a slightly steeper slope (indicated by the dashed grey line in the right panel of Figure 3) and marginally prefers a smaller σ , whereas the satellite analysis yields an equally good fit at all σ . In practice, the two regions may be combined to yield a single $\alpha(\sigma)$ relation, but we elect to consider them independently, both to include the isolated “pairs” in the left panel, which do not have analogous LF regions and therefore cannot be included in the right plot, and because the incompleteness is more poorly understood in the LF. The average best-fit α is well fit by a quadratic function in both cases. Specifically, for the satellites we find α :

$$\alpha_{\text{sats}} \cong 0.14\sigma^2 + 0.14\sigma + 1.79 \quad (5)$$

while the LF relation is best-fit by

$$\alpha_{\text{LF}} \cong 0.24\sigma^2 + 0.16\sigma + 1.99, \quad (6)$$

where σ is one standard deviation of the \log_{10} -normal scatter.

The symbols overplotted in Figure 3 indicate the results of B13 (black square), Garrison-Kimmel et al. (2014a, black diamond), and Moster et al. (2013, circles). Because the latter relation is derived assuming that abundance matching is performed at the redshift of a subhalo’s infall, we plot the evolution of the slope for $0 < z < 3$ in the left panel (dashed black line), with specific redshifts highlighted. Though there

is a large spread in the infall redshifts of the ELVIS subhalos, Wetzel et al. (2015) showed that most fell into a larger host between $3 \gtrsim z \gtrsim 0.5$. Nonetheless, the comparison to the Moster et al. (2013) slopes is imperfect due to differing normalizations; in practice, however, the Moster et al. (2013) normalization at $M_{\text{halo}} = 10^{11} M_\odot$ differs from that of B13 (and therefore our normalization) by less than 5% in logspace.

Figure 4 similarly illustrates the results for a model where the scatter grows with decreasing galaxy mass. As in Figure 3, the vertical axis shows the log-slope of $M_\star - M_{\text{peak}}$, but the horizontal axis here plots v , the slope of $\sigma(\log_{10} M_{\text{peak}})$ (see Equation 3). For reference, the upper axis indicates the symmetric scatter at $M_{\text{peak}} = 10^{10} M_\odot$, highlighting the fact that the growing scatter model explores larger scatters than the constant scatter case. The results, however, are qualitatively identical: as the scatter grows, α must also grow in order to avoid overproducing the observed SMF. The best-fit relation is here presented in terms of v :

$$\alpha_{v,\text{sats}} \cong 0.25v^2 - 1.37v + 1.69. \quad (7)$$

We do not plot the relation for the LF because it follows a qualitatively identical trend to Figure 4 with a slight offset to steeper slopes, as expected through comparison with Figure 3. Specifically, the best-fit log-slope α from the field galaxies is given by

$$\alpha_{v,\text{field}} \cong 0.47v^2 - 1.48v + 1.81. \quad (8)$$

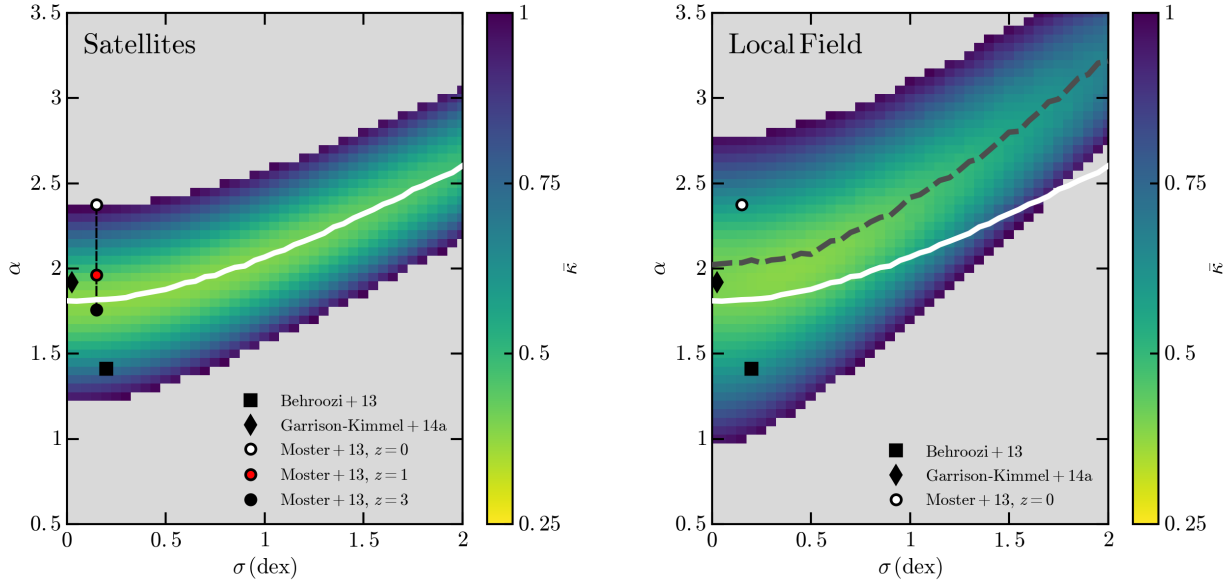


Figure 3. The goodness of fit, quantified by κ , of the subhalo mass functions to the MW and M31 stellar mass functions (left) and similarly for halos and galaxies in the Local Field (right), as a function of the log-slope α of the M_\star - M_{peak} relation and of the log-normal scatter σ about the median relation. Plotted are the averages over the systems, which are themselves averaged over 500 realizations for each combination of σ and α . The solid white line, which is the same in both panels, indicates the best-fit α derived from the satellite distribution. For the left plot, we minimize $\kappa_{\text{MW}} + \kappa_{\text{M31}}$ for each realization; i.e., each host may be matched with either the MW or M31. Plotted is $(\kappa_{\text{MW}} + \kappa_{\text{M31}})/2$, which weights the two satellite systems equally and consequently weights the individual MW satellites more heavily than the M31 satellites. As the assumed scatter increases, α must also increase such that the relation falls off more steeply for $M_{\text{peak}} < M_1 \sim 10^{11.5} M_\odot$. Otherwise, the scattering of small halos to high M_\star results in an over-estimation of the SMF. For comparison, we overplot the faint-end log-slopes quoted by B13 (black square), Garrison-Kimmel et al. (2014a, black diamond), and Moster et al. (2013, circles). Because the Moster et al. (2013) formalism dictates that satellite systems are assigned stellar masses based on both their infall mass and infall redshift, the left panel indicates the range of log-slopes quoted by Moster et al. (2013) for $0 < z < 3$. We caution, however, that the Moster et al. (2013) and B13 points represent extrapolations from higher stellar masses. We emphasize that a model that falls within the allowed band is not necessarily correct, but models that are purely power-laws for $M_\star \simeq 10^5 - 10^8 M_\odot$ that fall outside the allowed band will not, in general, reproduce the LG M_\star functions.

The difference in the preferred log-slopes between the satellite systems and the LF is likely to be enhanced by tidal effects from a baryonic disk, which will systematically shift the subhalo mass functions lower at fixed counts. Assuming that dark subhalos are destroyed at the same rate as luminous satellites, this shift will allow an even shallower $M_\star - M_{\text{halo}}$ relation to fit the satellite systems. The discrepancy between the LF and the satellite systems is further highlighted by extrapolating the the LF below the completeness limit: the best-fit relation at $\sigma = 0$ dex predicts an average of ~ 40 LF galaxies with $10^5 < M_\star/M_\odot < 10^6$ (“classical” dwarfs), which decreases to ~ 10 for $\sigma = 2$ dex. If upcoming surveys do not identify a wealth of new nearby field galaxies, it may be indicative of a change in how galaxy formation proceeds in small halos at late times, as satellites of a given mass today are likely to have formed earlier than field halos at the same mass.

Averaged over the twenty-four MW-M31 pairs or the nine LFs, the best-fit α yields a fit, quantified by κ , that is 3 – 4 times worse than the Monte Carlo realizations of the observational data with themselves. However, the single best-fit *realization* of each system, taken over all values of α at fixed σ , typically yield a fit that is only ~ 0.1 dex worse than the data with themselves, even after averaging over the systems. Moreover, merely selecting these best-fit

realizations at each σ yields log-slopes identical to the fits given above.

3.2 Implications for the too-big-to-fail problem

Having quantified the best-fit log-slope as a function of the scatter, we move to investigating how the severity of TBTF varies with σ . We quantify the problem by counting the number of massive dark matter halos that are missing from the known galaxy population. We call these missing massive systems “massive failures.” While Figure 3 indicates the trends with α and σ averaged over the ELVIS systems, in this section we will count massive failures for a given σ at the best-fit α of *each system*, averaging over the realizations of that system. Within 300 kpc of the MW, we then count massive failures in the host matched with the MW, again in a realization-by-realization manner.

Our definition of massive failures is similar to that employed in Garrison-Kimmel et al. (2014b) in that we select “candidate” (sub)halos to host the dwarf galaxies, then require that each dwarf be matched with only one (sub)halo. A dwarf may only be matched with a (sub)halo if the 1σ error on the implied circular velocity at the 3D half-light radius, $V_{1/2}$ at $R_{1/2}$, is greater than the circular velocity V_{circ} of that

sub(halo) at $R_{1/2}$. As in Garrison-Kimmel et al. (2014b), we calculate V_{circ} profiles for halos from V_{max} , the maximum circular velocity of the halo, and R_{max} , the radius at which V_{max} occurs, assuming Einasto (1965) profiles with a shape parameter of 0.18, which fits the density profiles of subhalos in ultra-high resolution simulations slightly better than the Navarro et al. (1997) profile (Springel et al. 2008b).⁷ Unlike Garrison-Kimmel et al. (2014b), however, we select candidate halos based not on their halo properties, but on the stellar masses that they were assigned in a given realization, such that all halos above the incompleteness limits ($4.5 \times 10^5 M_\odot$ around the MW and $4.5 \times 10^6 M_\odot$ in the LF) are eligible to be counted as massive failures. All remaining (sub)halos, i.e. those with M_\star above the completeness limit that are not assigned a galaxy, are considered massive failures. The average number of these massive failures in each realization is plotted in Figure 5, which we explain in greater detail below.

Our observational samples are comprised of the MW satellites and LF dwarfs listed in Table 1. As in previous TBTF analyses (e.g. Boylan-Kolchin et al. 2012; Garrison-Kimmel et al. 2014b), however, we eliminate the LMC and the SMC due both to their relative rarity and substantial contribution from baryons within $R_{1/2}$, and also exclude the Sagittarius dSph as it is currently interacting with the disk and is unlikely to be in kinematic equilibrium. For consistency, we therefore rank order the subhalos of each realization by their assigned M_\star and exclude the three largest, rather than simply excluding the three most massive (by dark matter mass). We also exclude NGC 6822 from our counting in the LF, as it is likewise baryon dominated within $R_{1/2}$ (Kirby et al. 2014), and Sagittarius dIrr, as there have thus far been no attempts to measure its internal kinematics. To match these exclusions, we similarly remove the halo with the highest M_\star and the halo with the sixth highest M_\star from each realization for the LF.

Kinematic data ($V_{1/2}$ and $R_{1/2}$) for the remaining nine MW satellites are drawn from Wolf et al. (2010), who used observational data from Muñoz et al. (2005); Koch et al. (2007); Simon & Geha (2007); Mateo et al. (2008) and Walker et al. (2009). We similarly apply the Wolf et al. (2010) formula to measurements taken by Kirby et al. (2014) for the purely dispersion supported galaxies in the LF. However, two of the LF galaxies included display evidence of additional rotational support. $V_{1/2}$ and $R_{1/2}$ for WLM are taken from (Leaman et al. 2012), and, following Weiner et al. (2006), we account for the rotation support of Pegasus dIrr by adding, in quadrature, the projected rotation velocity $v \sin i$ and the stellar velocity dispersion σ_{star} when using the Wolf et al. (2010) formula for $V_{1/2}$ (also see §5.2 of Kirby et al. 2014).

The results of this counting are summarized in the left and right panels of Figure 5 for the constant and growing scatter models, respectively. The upper panels plot the number of massive failures, either within 300 kpc of the MW (magenta lines) or in the LF (orange lines), as a function

⁷ As demonstrated in Garrison-Kimmel et al. (2014b), using the slightly lower density NFW profile reduces massive failure counts around the MW by $\sim 15\%$, but has a negligible effect in the Local Field.

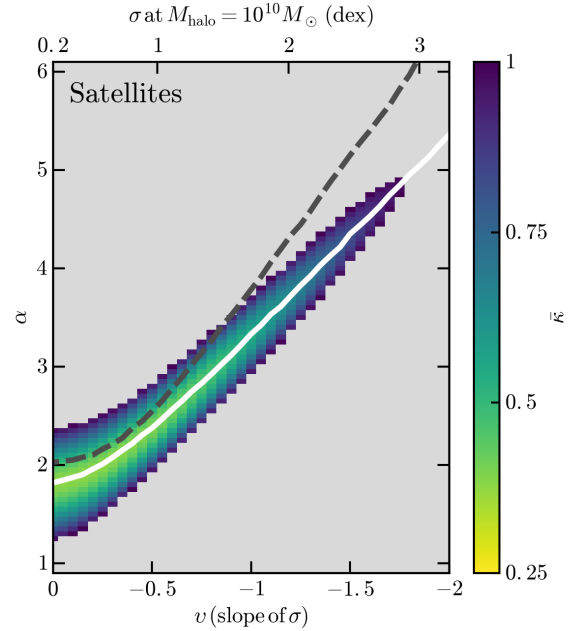


Figure 4. The goodness of fit between the MW/M31 SMFs and the mock satellite catalogs obtained by applying the growing scatter model to the ELVIS simulations. As in Figure 3, the y-axis indicates the assumed faint-end log-slope α . Here, however, the x-axis indicates v , the log-slope of σ (see Equation 3). For reference, the upper x-axis shows the resultant scatter at $M_{\text{peak}} = 10^{10} M_\odot$. The x-axis is inverted such that the scatter increases towards the right. As in the constant scatter model, a larger σ necessitates a more rapid fall-off in $M_\star(M_{\text{peak}})$ to avoid overproducing the observed SMFs. Because we explore even larger σ compared to the constant scatter model, however, we find even steeper slopes are required. As in Figure 3, the solid white and dashed grey lines represent the best-fit models in for the satellite and field systems, respectively.

of the assumed scatter σ (left panel) or the assumed log-slope of the scatter v (right panel), while the lower panels indicate the fraction of realizations with zero massive failures. Solid lines indicate the fiducial count, roughly comparable to Garrison-Kimmel et al. (2014b), while the dashed lines count massive failures after suppressing the V_{max} of every halo by $1 - \sqrt{1 - f_b} \sim 10\%$ to demonstrate a scenario wherein the baryonic contribution to the particle mass in the DM-only ELVIS simulations is removed from the potential, thereby partially capturing that dwarfs are typically far from baryonically closed (e.g. Wolf et al. 2010). As in Figures 3 and 4, the lines plot averages over the systems, which are themselves averaged over the realizations of that system. We do not count massive failures around the host matched with M31, but note that Tollerud et al. (2014) showed that TBTF is similarly extant among the M31 satellites.

The results of Figure 5 are striking, particularly for the satellites of the MW. On average, the number of massive failures decreases from ~ 8 and ~ 6 in the zero-scatter count, for the standard and gas-loss cases, down to $\sim 2 - 3$ for both cases when σ increases to 2 dex.⁸ Moreover, as seen

⁸ We note that there are significantly fewer massive failures

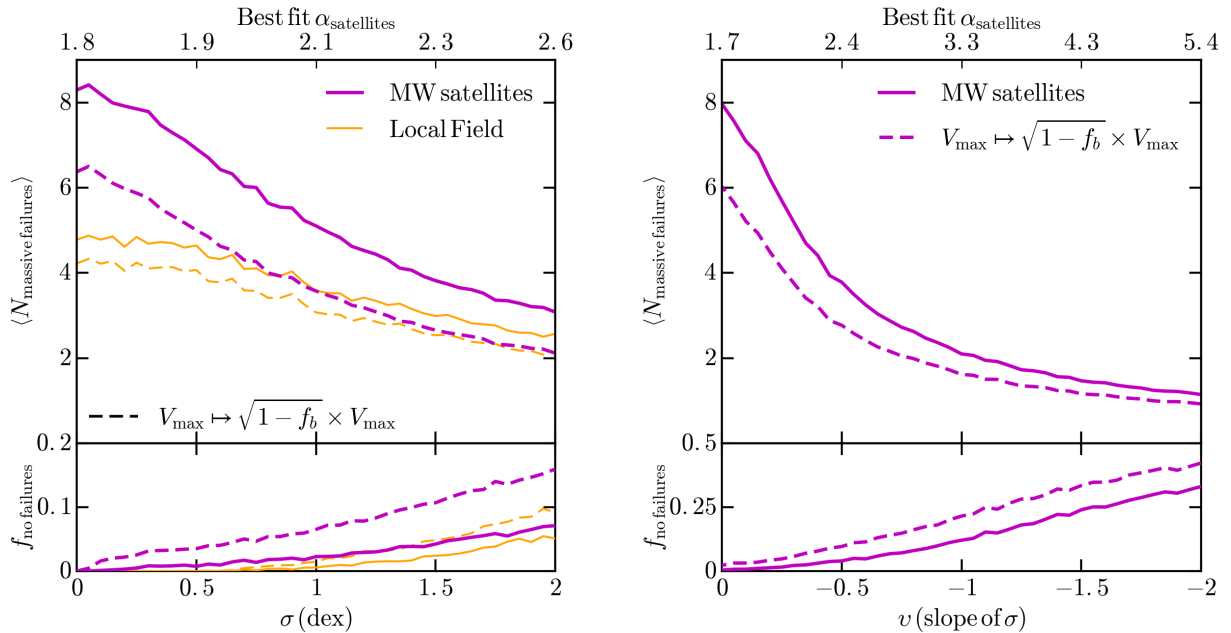


Figure 5. The number of massive failures, within 300 kpc of the MW in magenta and in the Local Field in green, as a function of the scatter at the best-fit α at the scatter in the constant scatter model (left) and the growing scatter model (right), plotted such that the magnitude of the scatter increases towards the right of each plot. Massive failures are defined as (sub)halos with M_* greater than the completeness limit ($4.5 \times 10^5 M_\odot$ in the MW, $4.49 \times 10^6 M_\odot$ in the Local Field) without observational counterparts (as in Garrison-Kimmel et al. 2014b), where the three brightest (by M_*) subhalos and the brightest and sixth brightest field halo in each realization are excluded, to match the observational cuts. The magenta lines plot the number of massive failures within 300 kpc of the MW, averaged over all 12 pairs and the 12 pseudo-pairs; the orange line averages over the fields of the nine pairs included in our analysis. For each realization, massive failures within 300 kpc are drawn from the subhalos of the host matched with the MW. The dashed lines indicate massive failure counts after suppressing the rotation curves of all halos by $\sqrt{1-f_b} \sim 0.91$ to mock the effects of a reduced particle mass in cosmological hydrodynamical simulations. As the scatter increases, the average number of massive failures within 300 kpc in the constant scatter model (growing scatter model) decreases by $\sim 2/3$ ($\sim 7/8$), and the fraction of realizations with no massive failures increases to $\sim 10\%$ ($\sim 40\%$). The field demonstrates a similar trend, such that $\sim 5\%$ of realizations are without massive failures in the constant scatter model.

in the bottom panels, the fraction of realizations that are completely devoid of massive failures increases steadily with increasing scatter. For 2 dex of scatter, we find that $\sim 15\%$ of realizations are completely without massive failures, once we account for the reduction in halo mass due strictly to the reduced mass of DM particles in cosmological hydrodynamical simulations. In the right-hand panel we see that the growing scatter model yields similar results.

Our method is designed to maintain a roughly equal number of halos (9 in the MW and 7 in the LF) with stellar masses large enough to be seen above the adopted completeness limits at all σ and v . This means that for low scatters (1) even the best-fit α overproduces the stellar mass function of the MW at low masses (see Figure 2) and (2) the vast majority ($\sim 60\%$ in the MW sample and $\sim 85\%$ in the LF) of halos above the completeness limit are massive failures. At high scatters, however, a larger portion of the theoretical sample is composed of small halos (hosting bright galaxies) that are more kinematically similar to the known dwarfs.

counted here than in Garrison-Kimmel et al. (2014b), who found ~ 15 massive failures in each LF. This is primarily due to the more stringent cuts that we have used in this work: only halos assigned enough stellar mass in a given realization to be above the completeness cut are eligible to be failures. In the previous work, we selected halos with peak $V_{\max} > 30 \text{ km s}^{-1}$.

Relations with very large scatter solve TBTF by occasionally assigning the largest halos a very small stellar mass – so small that they fall below the completeness limit. Effectively, these relations solve TBTF by demanding that the most massive halos do indeed fail to form stars appreciably. The $M_* - M_{\text{halo}}$ relation for one such realization ($\sigma = 2$ dex) is plotted explicitly in the left panel of Figure 6 as black circles; the median relation is indicated by the cyan line. The open points plot subhalos that lie below the completeness limit of the MW (indicated by the lower edge of the shaded band), and which are therefore ineligible to be massive failures. This realization does not exhibit the TBTF problem because many of the largest subhalos are assigned to host ultra-faint dwarf galaxies, which we assume are unobservable. By contrast, the best-fit zero-scatter relation (magenta line) predicts that multiple high-mass subhalos host galaxies that lie above the completeness cut, and would therefore be counted as massive failures.

The right panel of Figure 6 shows the two $M_* - M_{\text{halo}}$ models presented in the left panel along with a summary of recent predictions from high-resolution hydrodynamic simulations. The black lines, which are extrapolated as gray lines below the dotted horizontal line at $M_* = 10^5 M_\odot$, the smallest M_* cut adopted, again represent the best-fit models for $\sigma = 0$ (dashed line) and $\sigma = 2$ dex (solid line, with shading to indicate σ and 2σ), but the points listed in the lower-left

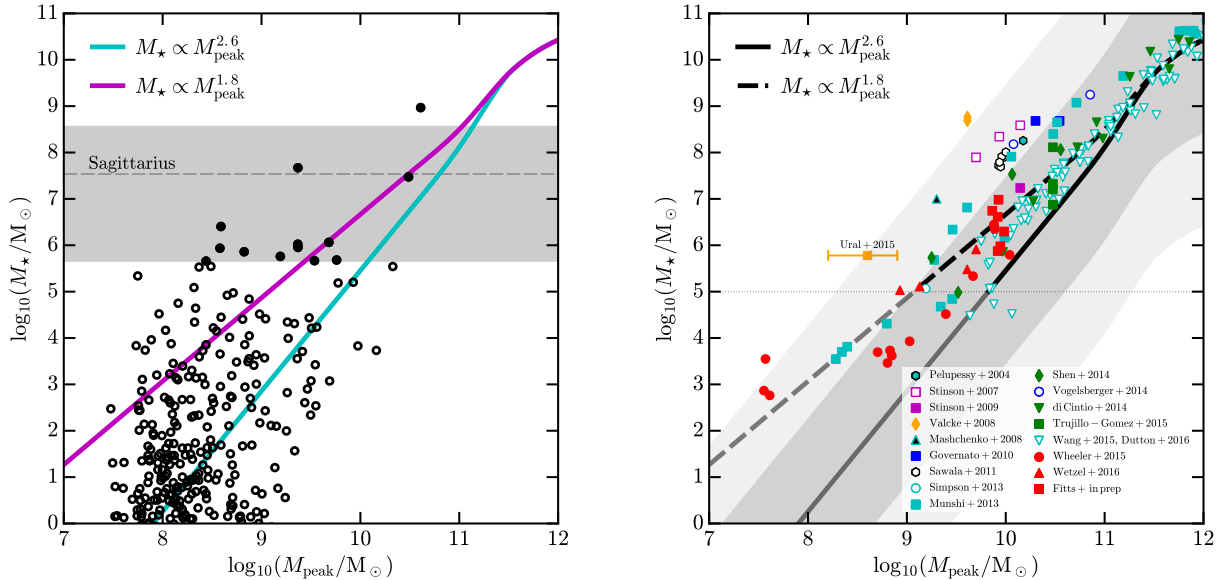


Figure 6. *Left:* A sample realization of the MW satellite system, obtained by applying the best-fit $\sigma = 2$ dex relation (black circles); the median relation is indicated by the cyan line. For comparison, the magenta line plots the best-fit zero-scatter relation. The shaded region roughly indicates the range in stellar masses probed by our method in the MW (constraints from M31 extend to $10^5 M_\odot$). The upper edge of this regime is here set by the stellar mass of the SMC, but in general is defined by the second highest M_\star in each realization. Subhalos that fall below the completeness limit are indicated by open circles. The horizontal dashed line indicates the stellar mass of Sagittarius, which roughly sets the upper limit on the massive failure sample (the exact limit is set by the third most luminous subhalo in each realization; see § 3.2); subhalos that fall between this limit and the lower edge of the shaded band are eligible to be massive failures. The 2 dex case, selected because it has no massive failures, illustrates how scatter in $M_\star - M_{\text{halo}}$ is able to alleviate TBTF: many of the most massive subhalos, which have internal kinematics inconsistent with the MW dSphs, are assigned to host ultra-faint dwarf galaxies that lie in the incomplete regime, and are therefore excluded from the analysis. *Right:* A comparison of the same two best-fit relations (black lines, which become gray when extrapolated beyond the regime constrained by our analysis in either the MW or M31, $M_\star < 10^5 M_\odot$, a limit that is also indicated by the horizontal dashed line) to a sample of simulated dwarf galaxies in the literature (references are as indicated in the legend); the shaded regions indicate one and two standard deviations. If the simulations trace the best-fit zero-scatter relation (dashed line), then the level of scatter exhibited overall will generally overproduce the local SMFs. Alternatively, if the simulations trace the upward scatter about the 2 dex relation, which aids in resolving TBTF, then they thus far fail to sample the downward scatter necessary to avoid overproducing the local SMFs. Taken independently, many of the simulation suites targeting isolated dwarfs, including Munshi et al. (2013), NIHAO (Wang et al. 2015; Dutton et al. 2016), and those simulated with the FIRE physics (Hopkins et al. 2014; Wheeler et al. (2015); Wetzel et al. (2016), and Fitts et al. (in preparation), may be sampling a relatively low-scatter relation (with $\sigma < 0.5$ dex) that would generally reproduce LG counts. However, a larger sample of halos, particularly with $M_{\text{peak}} < 10^{10} M_\odot$, is necessary to make quantitative statements about the behavior of simulations in this regime, where constraints remain weak relative to higher M_\star . The Ural et al. (2015) point (orange square with error bars), which is derived from combining N-body simulations with MCMC modeling, represents a potential constraint on Carina and is discussed in § 4.

indicate the results of baryonic simulations that include both star formation and feedback (Pelupessy et al. 2004; Stinson et al. 2007; Valcke et al. 2008; Mashchenko et al. 2008; Stinson et al. 2009; Governato et al. 2010; Sawala et al. 2011; Simpson et al. 2013; Munshi et al. 2013; Shen et al. 2014; Vogelsberger et al. 2014; di Cintio et al. 2014; Trujillo-Gomez et al. 2015; Wang et al. 2015; Dutton et al. 2016; Wheeler et al. 2015; Wetzel et al. 2016, Fitts et al. in preparation).

Though the simulations adopt a range of baryonic prescriptions, it is immediately obvious that, taken together, they qualitatively fail to uniformly sample the $\sigma = 2$ dex relation. Specifically, only the NIHAO simulations form low-mass galaxies in $M_{\text{peak}} 10^{10} M_\odot$ hosts, which is what is required to solve TBTF via scatter alone. Alternatively, if the simulations trace a flatter relation, then the scatter about that relation is too large to avoid overproducing the SMFs with low-mass halos hosting bright dwarfs. We caution, how-

ever, that much of the apparent scatter is due to variations among different codes. Many of the individual simulations produce relations that are rather tight on their own, and several may reproduce LG galaxy counts if applied to an LG-like volume. However, more high-resolution simulations targeting halos with $M_{\text{peak}} \lesssim 10^{10} M_\odot$ are needed to fully quantify the behavior of any of these codes in this regime.

4 DISCUSSION

Our results highlight the importance of understanding the nature of the $M_\star - M_{\text{halo}}$ relation at low masses. They also indicate that, if the $M_\star - M_{\text{halo}}$ relation behaves as a power-law with scatter at low M_\star , pinpointing the degree of either the scatter or the slope of the median relation should provide clues to the other, though it may be impossible to disentangle the two. Moreover, the level of scatter has

clear consequences on current small-scale problems in the Λ cold dark matter (ACDM) paradigm of galaxy formation. Specifically, a high scatter results in a significant fraction of satellite and LF systems wherein the majority of the massive ($M_{\text{halo}} \sim 10^{10.5} M_{\odot}$) halos preferentially scatter downward in stellar mass, thereby alleviating TBTF by assigning the typically problematic halos to host ultra-faint dwarf galaxies. This requires a steep fall-off in the median relation, however. Furthermore, the required scatter is very high: for $\sigma = 2$ dex, 5% of (sub)halos will host galaxies that lie a factor of 10^4 from the median relation.

Ultimately, however, it is extremely difficult to determine whether the rapid variability of the instantaneous specific star formation rate predicted in simulations (e.g. [Oñorbe et al. 2015](#); [Wetzel et al. 2016](#)) and the sensitivity to mass accretion discussed in § 1 truly does result in $\gtrsim 2$ dex of scatter in M_{\star} at fixed M_{halo} in the dwarf regime. A conclusive answer would require not only an enormous sample of dwarf galaxies in the field, where DM halos have not been stripped by larger hosts, but measurements of the *halo* masses of each of those dwarfs. It would therefore be necessary to trace the mass well beyond the stars, or to firmly understand the density profiles of dwarfs such that measurements on small radii can accurately be extrapolated to the virial radius.

Recently, [Ural et al. \(2015\)](#) demonstrated an alternative approach by running idealized N-body simulations to model Carina ($M_{\star} = 6.03 \times 10^5 M_{\odot}$), wrapped within an MCMC pipeline to marginalize over the parameters of the initial conditions, including the pre-infall (peak) halo mass. Applying this method to a large number of MW and M31 satellites could potentially provide valuable insights into the shape and scatter of $M_{\star} - M_{\text{halo}}$. Their result, which is plotted in Figure 6 as an orange square and which agrees well with results of likelihood-based comparisons with high-resolution cosmological simulations ([Boylan-Kolchin et al. 2012](#)), places Carina well above the best-fit $\sigma = 0$ relation. It may therefore be a ~ 2 standard deviation outlier from the $\sigma = 2$ relationship.

Large scatter in $M_{\star} - M_{\text{halo}}$ may also be inferred from the properties of known galaxies in the MW. For example, [Wheeler et al. \(2015\)](#) identified a mass-dependent cutoff in post-reionization star formation in cosmological simulations: only halos larger than $\sim 5 \times 10^9 M_{\odot}$ are able to retain their gas in the presence of a reionizing background and continue to form stars beyond $z \sim 6$. Taken together with the results of [Brown et al. \(2014\)](#), who showed that six of the MW ultra-faint ($M_{\star} \sim 10^4 M_{\odot}$) satellites are dominated by stars older than 12 Gyr, one may easily conclude that the ultrafaint galaxies live in halos smaller than $M_{\text{halo}} \sim 5 \times 10^9 M_{\odot}$. A large scatter about the median relation, however, would result in several ultra-faints residing in large dwarfs. This scatter may therefore manifest in the form of ultra-faint dwarf galaxies with extended star formation histories. As was recently shown by [Monelli et al. \(2016\)](#), Andromeda XVI may be one such system. We may also expect to find faint, dense galaxies living at the centers of halos too massive to be altered by the small number of feedback events from those galaxies.

Our conclusions are largely similar to those of [Guo et al. \(2015\)](#), who applied semi-analytic galaxy formation models to DM-only simulations, then selected hosts analogous to

the MW based on the observable properties of the system. Their models predict highly stochastic galaxy formation at small mass scales, yielding a large scatter in the stellar mass-halo mass relation, such that $\sim 10\%$ of their satellite systems have only three bright halos with $V_{\text{max}} > 30$ km/s. Likewise, we find that $\sim 10\%$ of the ELVIS realizations contain a MW without any massive failures, assuming a scatter of 2 dex.

We caution that our analysis has ignored errors in the stellar masses of the dwarf galaxies. If these errors are systematically correlated such that the majority of the stellar masses are underestimated (overestimated), our best-fit α overestimates (underestimates) the true log-slope at a given scatter. Furthermore, while [B13](#) demonstrated that a single $M_{\star} - M_{\text{peak}}$ relation describes centrals and satellites well, it is in principle possible that the relationship varies with environment. If so, simulations of isolated dwarfs (i.e. those far from any MW-size hosts) should not necessarily match the best-fit $\alpha(\sigma)$ derived here. However, assuming an $M_{\star}(M_{\text{peak}}) \propto M_{\star}^{\alpha}$ that is independent of environment and that behaves like a pure power-law in the stellar mass regime explored here, such simulations should approximately match the results presented here in order to reproduce galaxy counts in the LG. Finally, we explicitly note that our models are *not* expected to hold for $M_{\star} \gtrsim 10^9 M_{\odot}$, where large-volume surveys have constrained the scatter to be $\sigma \lesssim 0.2$ dex.

5 CONCLUSIONS

In this work, we have explored two-parameter models for assigning stars to low-mass ($M_{\text{halo}} \lesssim 10^{11} M_{\odot}$) dark matter halos in the collisionless ELVIS simulations. We fix the $M_{\star} - M_{\text{halo}}$ relation to that of [Behroozi et al. \(2013c\)](#) for $M_{\text{halo}} \gtrsim 10^{11} M_{\odot}$ and allow the scatter σ in this relation to vary between 0 and 2 dex, then constrain the best-fit log-slope α . Briefly, we find that:

- As the assumed scatter increases, the median relation must become increasingly steep to avoid overproducing the observed stellar mass functions of the MW, M31, and the nearby Local Field.

- The best-fit log-slope α is significantly steeper than the $z = 0$ slope predicted by [B13](#), which overproduces local galaxy counts (see [Garrison-Kimmel et al. 2014a](#)). In contrast, the best-fit zero-slope relation nearly matches that predicted in [Garrison-Kimmel et al. \(2014a\)](#), who derived α from the faint-end slope of the SMF measured by the GAMA survey ([Baldry et al. 2012](#)). Finally, we find slightly shallower log-slopes than those quoted by [Moster et al. \(2013\)](#), particularly at $z = 0$, even when compared to the field. However, their log-slope at $z \sim 1$, roughly the median infall redshift of subhalos around MW-size hosts ([Wetzel et al. 2015](#)), is only slightly steeper than our measured best-fit α_{sats} .

- At the best-fit α , the average number of massive failures, both within 300 kpc of the MW and in the LF, decreases with increasing σ . After mocking the effects of baryonic mass loss, we find that the MW satellite system may be only a $\sim 15\%$ outlier, if there are ~ 2 decades of scatter about the median $M_{\star} - M_{\text{halo}}$ relation.

- Mass-dependent scatter produces qualitatively similar results to mass-independent models but leads to even steeper relations for an equivalent scatter at $M_{\text{peak}} = 10^{10} M_{\odot}$, as

smaller galaxies are more likely to appear in the complete regime for growing scatter models.

- Currently, simulations are able to reproduce the upward scatter that solves TBTF (by placing bright galaxies in small halos), but overall, are thus far unable to reproduce the downward scatter (placing faint galaxies in overly-massive halos) necessary to avoid overproducing the observed stellar mass functions. However, this ignores changes to the internal structure of (sub)halos and furthermore assumes that $M_\star(M_{\text{halo}})$ can be modeled as scatter about a median power-law.

Our results provide a method for simulators to check whether their resultant $M_\star - M_{\text{halo}}$ relation can match counts in the LG. Specifically, simulators should 1) fit a power-law to $M_\star - M_{\text{peak}}$, normalized to the relation in Equation 1, to find α ; 2) measure the scatter about that relation to determine σ and; 3) compare with the constraints in Figure 3. If $M_\star - M_{\text{peak}}$ is well-fit by a power-law, but the resultant (α, σ) lies well outside the contours provided here, then the simulations will not reproduce galaxy counts in the LG. Simulations that are not well fit by a power-law in M_{peak} are not constrained by our method.

Our results are largely independent of the exact model used to set M_\star , and hold for the constant and growing scatter models. Together, they suggest that scatter in $M_\star - M_{\text{halo}}$ alone is unlikely to explain the TBTF problem, but that it may contribute to the eventual solution, along with ram-pressure stripping and internal feedback processes. Nonetheless, it is encouraging for the Λ CDM paradigm of galaxy formation that scatter in $M_\star - M_{\text{halo}}$, which simulations predict to at least some degree, helps to eliminate the massive failures. As yet, however, there remains no direct evidence for the required scatter.

Acknowledgments

The authors thank Michael Cooper, Marla Geha, Coral Wheeler, Jose Oñorbe, Ferah Munshi, Erik Tollerud, Frank van den Bosch, Andrew Wetzel, Massimo Ricotti, Phil Hopkins, Justin Read, and the anonymous referee for valuable comments that have improved the manuscript. We also thank Aaron Dutton for providing the NIHAO data.

Support for SGK was provided by NASA through Einstein Postdoctoral Fellowship grant number PF5-160136 awarded by the Chandra X-ray Center, which is operated by the Smithsonian Astrophysical Observatory for NASA under contract NAS8-03060. MBK acknowledges support from the National Science Foundation (grant AST-1517226) and from NASA through HST theory grants (programs AR-12836 and AR-13888) awarded by the Space Telescope Science Institute (STScI), which is operated by the Association of Universities for Research in Astronomy (AURA), Inc., under NASA contract NAS5-26555.

We also acknowledge the support of the *Greenplanet* cluster at UCI, where much of the analysis was performed. This work also made use of `matplotlib` (Hunter 2007), `Astropy` (Astropy Collaboration et al. 2013), `numpy` (van der Walt et al. 2011), `scipy` (Jones et al. 01), and `ipython` (Perez & Granger 2007). This research has made use of NASA's Astrophysics Data System.

References

- Amorisco N. C., Zavala J., de Boer T. J. L., 2014, *ApJ*, **782**, L39
- Anderhalden D., Schneider A., Macciò A. V., Diemand J., Bertone G., 2013, *J. Cosmology Astropart. Phys.*, **3**, 14
- Arraki K. S., Klypin A., More S., Trujillo-Gomez S., 2014, *MNRAS*, **438**, 1466
- Astropy Collaboration et al., 2013, *A&A*, **558**, A33
- Baldry I. K., et al., 2012, *MNRAS*, **421**, 621
- Behroozi P. S., Wechsler R. H., Wu H.-Y., 2013a, *ApJ*, **762**, 109
- Behroozi P. S., Wechsler R. H., Wu H.-Y., Busha M. T., Klypin A. A., Primack J. R., 2013b, *ApJ*, **763**, 18
- Behroozi P. S., Wechsler R. H., Conroy C., 2013c, *ApJ*, **770**, 57
- Bell E. F., de Jong R. S., 2001, *ApJ*, **550**, 212
- Benson A. J., Cole S., Frenk C. S., Baugh C. M., Lacey C. G., 2000, *MNRAS*, **311**, 793
- Berlind A. A., Weinberg D. H., 2002, *ApJ*, **575**, 587
- Blumenthal G. R., Faber S. M., Primack J. R., Rees M. J., 1984, *Nature*, **311**, 517
- Boylan-Kolchin M., Springel V., White S. D. M., Jenkins A., Lemson G., 2009, *MNRAS*, **398**, 1150
- Boylan-Kolchin M., Springel V., White S. D. M., Jenkins A., 2010, *MNRAS*, **406**, 896
- Boylan-Kolchin M., Bullock J. S., Kaplinghat M., 2011, *MNRAS*, **415**, L40
- Boylan-Kolchin M., Bullock J. S., Kaplinghat M., 2012, *MNRAS*, **422**, 1203
- Bozek B., Boylan-Kolchin M., Horiuchi S., Garrison-Kimmel S., Abazajian K., Bullock J. S., 2016, *MNRAS*, **459**, 1489
- Brook C. B., Di Cintio A., Knebe A., Gottlöber S., Hoffman Y., Yepes G., Garrison-Kimmel S., 2014, *ApJ*, **784**, L14
- Brooks A. M., Zolotov A., 2014, *ApJ*, **786**, 87
- Brooks A. M., Kuhlen M., Zolotov A., Hooper D., 2013, *ApJ*, **765**, 22
- Brown T. M., et al., 2014, *Mem. Soc. Astron. Italiana*, **85**, 493
- Bullock J. S., Kravtsov A. V., Weinberg D. H., 2000, *ApJ*, **539**, 517
- Bullock J. S., Wechsler R. H., Somerville R. S., 2002, *MNRAS*, **329**, 246
- Busha M. T., Wechsler R. H., Behroozi P. S., Gerke B. F., Klypin A. A., Primack J. R., 2011, *ApJ*, **743**, 117
- Chan T. K., Kereš D., Oñorbe J., Hopkins P. F., Muratov A. L., Faucher-Giguère C.-A., Quataert E., 2015, *MNRAS*, **454**, 2981
- Conroy C., Wechsler R. H., Kravtsov A. V., 2006, *ApJ*, **647**, 201
- Del Popolo A., Lima J. A. S., Fabris J. C., Rodrigues D. C., 2014, *J. Cosmology Astropart. Phys.*, **4**, 021
- Dutton A. A., Macciò A. V., Frings J., Wang L., Stinson G. S., Penzo C., Kang X., 2016, *MNRAS*, **457**, L74
- Einasto J., 1965, *Trudy Astrofizicheskogo Instituta Alma-Ata*, **5**, 87
- Elbert O. D., Bullock J. S., Garrison-Kimmel S., Rocha M., Oñorbe J., Peter A. H. G., 2015, *MNRAS*, **453**, 29
- Garrison-Kimmel S., Rocha M., Boylan-Kolchin M., Bullock J. S., Lally J., 2013, *MNRAS*, **433**, 3539
- Garrison-Kimmel S., Boylan-Kolchin M., Bullock J. S., Lee

- K., 2014a, *MNRAS*, **438**, 2578
- Garrison-Kimmel S., Boylan-Kolchin M., Bullock J. S., Kirby E. N., 2014b, *MNRAS*, **444**, 222
- Garrison-Kimmel S., Horiuchi S., Abazajian K. N., Bullock J. S., Kaplinghat M., 2014c, *MNRAS*, **444**, 961
- Gnedin O. Y., Zhao H., 2002, *MNRAS*, **333**, 299
- Governato F., et al., 2010, *Nature*, **463**, 203
- Governato F., et al., 2012, *MNRAS*, **422**, 1231
- Gritschneder M., Lin D. N. C., 2013, *ApJ*, **765**, 38
- Guo Q., Cooper A. P., Frenk C., Helly J., Hellwing W. A., 2015, *MNRAS*, **454**, 550
- Hahn O., Abel T., 2011, *MNRAS*, **415**, 2101
- Hopkins P. F., Kereš D., Oñorbe J., Faucher-Giguère C.-A., Quataert E., Murray N., Bullock J. S., 2014, *MNRAS*, **445**, 581
- Horiuchi S., Bozek B., Abazajian K. N., Boylan-Kolchin M., Bullock J. S., Garrison-Kimmel S., Onorbe J., 2016, *MNRAS*, **456**, 4346
- Hunter J. D., 2007, *Computing In Science & Engineering*, **9**, 90
- Jiang F., van den Bosch F. C., 2015, *MNRAS*, **453**, 3575
- Jones E., Oliphant T., Peterson P., et al., 2001–, SciPy: Open source scientific tools for Python, <http://www.scipy.org/>
- Kirby E. N., Bullock J. S., Boylan-Kolchin M., Kaplinghat M., Cohen J. G., 2014, *MNRAS*, **439**, 1015
- Klypin A., Gottlöber S., Kravtsov A. V., Khokhlov A. M., 1999, *ApJ*, **516**, 530
- Koch A., Kleya J. T., Wilkinson M. I., Grebel E. K., Gilmore G. F., Evans N. W., Wyse R. F. G., Harbeck D. R., 2007, *AJ*, **134**, 566
- Kravtsov A. V., Berlind A. A., Wechsler R. H., Klypin A. A., Gottlöber S., Allgood B., Primack J. R., 2004, *ApJ*, **609**, 35
- Kravtsov A., Vikhlinin A., Meshcheryakov A., 2014, preprint, ([arXiv:1401.7329](https://arxiv.org/abs/1401.7329))
- Larson D., et al., 2011, *ApJS*, **192**, 16
- Leaman R., et al., 2012, *ApJ*, **750**, 33
- Lovell M. R., Frenk C. S., Eke V. R., Jenkins A., Gao L., Theuns T., 2014, *MNRAS*, **439**, 300
- Martin N. F., de Jong J. T. A., Rix H.-W., 2008, *ApJ*, **684**, 1075
- Mashchenko S., Wadsley J., Couchman H. M. P., 2008, *Science*, **319**, 174
- Mateo M., Olszewski E. W., Walker M. G., 2008, *ApJ*, **675**, 201
- Maxwell A. J., Wadsley J., Couchman H. M. P., 2015, *ApJ*, **806**, 229
- McConnachie A. W., 2012, *AJ*, **144**, 4
- McConnachie A. W., Irwin M. J., Ferguson A. M. N., Ibata R. A., Lewis G. F., Tanvir N., 2005, *MNRAS*, **356**, 979
- Monelli M., et al., 2016, *ApJ*, **819**, 147
- Moster B. P., Naab T., White S. D. M., 2013, *MNRAS*, **428**, 3121
- Muñoz R. R., et al., 2005, *ApJ*, **631**, L137
- Munshi F., et al., 2013, *ApJ*, **766**, 56
- Navarro J. F., Frenk C. S., White S. D. M., 1996, *ApJ*, **462**, 563
- Navarro J. F., Frenk C. S., White S. D. M., 1997, *ApJ*, **490**, 493
- Oñorbe J., Boylan-Kolchin M., Bullock J. S., Hopkins P. F., Kereš D., Faucher-Giguère C.-A., Quataert E., Murray N., 2015, *MNRAS*, **454**, 2092
- Papastergis E., Shankar F., 2016, *A&A*, **591**, A58
- Papastergis E., Giovanelli R., Haynes M. P., Shankar F., 2015, *A&A*, **574**, A113
- Peñarrubia J., Pontzen A., Walker M. G., Koposov S. E., 2012, *ApJ*, **759**, L42
- Pelupessy F. I., van der Werf P. P., Icke V., 2004, *A&A*, **422**, 55
- Perez F., Granger B. E., 2007, *Computing in Science Engineering*, **9**, 21
- Polisensky E., Ricotti M., 2014, *MNRAS*, **437**, 2922
- Pontzen A., Governato F., 2012, *MNRAS*, **421**, 3464
- Purcell C. W., Zentner A. R., 2012, *J. Cosmology Astropart. Phys.*, **12**, 7
- Read J. I., Gilmore G., 2005, *MNRAS*, **356**, 107
- Read J. I., Wilkinson M. I., Evans N. W., Gilmore G., Kleya J. T., 2006, *MNRAS*, **367**, 387
- Read J. I., Agertz O., Collins M. L. M., 2016a, *MNRAS*, **459**, 2573
- Read J. I., Iorio G., Agertz O., Fraternali F., 2016b, *MNRAS*, **462**, 3628
- Reddick R. M., Wechsler R. H., Tinker J. L., Behroozi P. S., 2013, *ApJ*, **771**, 30
- Rocha M., Peter A. H. G., Bullock J. S., Kaplinghat M., Garrison-Kimmel S., Oñorbe J., Moustakas L. A., 2013, *MNRAS*, **430**, 81
- Rodríguez-Puebla A., Avila-Reese V., Drory N., 2013, *ApJ*, **773**, 172
- Sawala T., Guo Q., Scannapieco C., Jenkins A., White S., 2011, *MNRAS*, **413**, 659
- Sawala T., et al., 2016, *MNRAS*, **456**, 85
- Shen S., Madau P., Conroy C., Governato F., Mayer L., 2014, *ApJ*, **792**, 99
- Simon J. D., Geha M., 2007, *ApJ*, **670**, 313
- Simpson C. M., Bryan G. L., Johnston K. V., Smith B. D., Mac Low M.-M., Sharma S., Tumlinson J., 2013, *MNRAS*, **432**, 1989
- Somerville R. S., 2002, *ApJ*, **572**, L23
- Springel V., 2005, *MNRAS*, **364**, 1105
- Springel V., et al., 2008a, *MNRAS*, **391**, 1685
- Springel V., et al., 2008b, *MNRAS*, **391**, 1685
- Stinson G. S., Dalcanton J. J., Quinn T., Kaufmann T., Wadsley J., 2007, *ApJ*, **667**, 170
- Stinson G. S., Dalcanton J. J., Quinn T., Gogarten S. M., Kaufmann T., Wadsley J., 2009, *MNRAS*, **395**, 1455
- Strigari L. E., Bullock J. S., Kaplinghat M., Simon J. D., Geha M., Willman B., Walker M. G., 2008, *Nature*, **454**, 1096
- Tollerud E. J., Boylan-Kolchin M., Barton E. J., Bullock J. S., Trinh C. Q., 2011, *ApJ*, **738**, 102
- Tollerud E. J., et al., 2012, *ApJ*, **752**, 45
- Tollerud E. J., Boylan-Kolchin M., Bullock J. S., 2014, *MNRAS*, **440**, 3511
- Trujillo-Gomez S., Klypin A., Colín P., Ceverino D., Arraki K. S., Primack J., 2015, *MNRAS*, **446**, 1140
- Ural U., Wilkinson M. I., Read J. I., Walker M. G., 2015, *Nature Communications*, **6**, 7599
- Valcke S., de Rijcke S., Dejonghe H., 2008, *MNRAS*, **389**, 1111
- Vera-Ciro C. A., Helmi A., Starkenburg E., Breddels M. A., 2013, *MNRAS*, **428**, 1696
- Vogelsberger M., Zavala J., Loeb A., 2012, *MNRAS*, **423**,

3740

- Vogelsberger M., Zavala J., Simpson C., Jenkins A., 2014, [MNRAS](#), **444**, 3684
- Walker M. G., Mateo M., Olszewski E. W., 2009, [AJ](#), **137**, 3100
- Wang J., Frenk C. S., Navarro J. F., Gao L., Sawala T., 2012, [MNRAS](#), **424**, 2715
- Wang L., Dutton A. A., Stinson G. S., Macciò A. V., Penzo C., Kang X., Keller B. W., Wadsley J., 2015, [MNRAS](#), **454**, 83
- Weiner B. J., et al., 2006, [ApJ](#), **653**, 1027
- Wetzel A. R., Deason A. J., Garrison-Kimmel S., 2015, [ApJ](#), **807**, 49
- Wetzel A. R., Hopkins P. F., Kim J.-h., Faucher-Giguère C.-A., Kereš D., Quataert E., 2016, [ApJ](#), **827**, L23
- Wheeler C., Oñorbe J., Bullock J. S., Boylan-Kolchin M., Elbert O. D., Garrison-Kimmel S., Hopkins P. F., Kereš D., 2015, [MNRAS](#), **453**, 1305
- White S. D. M., Rees M. J., 1978, [MNRAS](#), **183**, 341
- Wolf J., Martinez G. D., Bullock J. S., Kaplinghat M., Geha M., Muñoz R. R., Simon J. D., Avedo F. F., 2010, [MNRAS](#), **406**, 1220
- Woo J., Courteau S., Dekel A., 2008, [MNRAS](#), **390**, 1453
- Zavala J., Vogelsberger M., Walker M. G., 2013, [MNRAS](#), **431**, L20
- Zolotov A., et al., 2012, [ApJ](#), **761**, 71
- di Cintio A., Knebe A., Libeskind N. I., Yepes G., Gottlöber S., Hoffman Y., 2011, [MNRAS](#), **417**, L74
- di Cintio A., Brook C. B., Macciò A. V., Stinson G. S., Knebe A., Dutton A. A., Wadsley J., 2014, [MNRAS](#), **437**, 415
- van der Walt S., Colbert S. C., Varoquaux G., 2011, [Computing in Science Engineering](#), **13**, 22